Sustainable Chemistry

International Edition: DOI: 10.1002/anie.201503346
German Edition: DOI: 10.1002/ange.201503346

# Single-Crystal Semiconductors with Narrow Band Gaps for Solar Water Splitting

*Tuo Wang and Jinlong Gong**

hydrogen · semiconductors · single crystals · solar water splitting · sustainable chemistry

*Solar water splitting provides a clean and renewable approach to produce hydrogen energy. In recent years, single-crystal semiconductors such as Si and InP with narrow band gaps have demonstrated excellent performance to drive the half reactions of water splitting through visible light due to their suitable band gaps and low bulk recombination. This Minireview describes recent research advances that successfully overcome the primary obstacles in using these semiconductors as photoelectrodes, including photocorrosion, sluggish reaction kinetics, low photovoltage, and unfavorable planar substrate surface. Surface modification strategies, such as surface protection, cocatalyst loading, surface energetics tuning, and surface texturization are highlighted as the solutions.*

## 1. Introduction

Since the pioneering work of Honda and Fujishima using single-crystal n-$TiO_2$ (001) photoanode in 1972,[1] photoelectrochemical (PEC) water splitting has received considerable attention. Overall water splitting is an energetically uphill process that includes a hydrogen evolution reaction (HER) and an oxygen evolution reaction (OER), accompanied by a positive change in the Gibbs free energy ($\Delta G = 237.3\ kJ\,mol^{-1}$ or 1.23 eV per electron under standard conditions).[2] Thus, the band gap of a semiconductor should be large enough to straddle the HER and OER potentials (0 and 1.23 V vs. normal hydrogen electrode, NHE, respectively, at pH 0) to achieve unassisted solar water splitting.

Alternatively, a hydrogen-evolving photocathode and an oxygen-evolving photoanode can be connected in series as a tandem device, as in the Z-Scheme water splitting except that external circuits instead of reversible redox shuttles are used to connect the two electrodes.[3] In such dual-absorber tandem cell configuration, semiconductors with narrow band gaps (i.e., 1.1–1.7 eV) can be used for improved light absorption, while maintaining the thermodynamic requirement of 1.23 eV to split water by coupling the photovoltages generated by the two electrodes.

With the 1.23 eV band-gap requirement lifted, it is possible to design tandem PEC water splitting electrodes using semiconductors with a mature substrate manufacturing infrastructure. Among them, Si is an extremely attractive candidate owing to its narrow band gap (1.1 eV), earth abundancy and wide applications in the photovoltaics and microelectronics industries with a vast knowledge base.[4] As a direct band-gap III-V semiconductor, InP is also an attractive candidate due to its suitable band gap (1.3 eV), appropriate band edge position, and low surface recombination velocity.[5] Highly active single-crystal InP-based photocathodes were demonstrated by Heller and Vadimsky with an appreciable solar-to-hydrogen efficiency of 12% in 1981.[6] Turner et al. further significantly advanced the performance of III-V semiconductor-based photoelectrode by coupling a bottom GaAs (1.42 eV) photovoltaic cell with a top $GaInP_2$ (1.83 eV) PEC cell, which realized unassisted water splitting with a remarkable $H_2$ production efficiency of 12.4%.[7] Subsequently, Licht et al. have shown that it is possible to perform solar water splitting with an AlGaAs/Si tandem photoelectrolysis cell at an extraordinary energy conversion efficiency of 18.3%.[8]

In terms of the quality of the semiconductor, single-crystal substrates without grain boundaries could offer unique

[*] Assoc. Prof. Dr. T. Wang, Prof. Dr. J. Gong
Key Laboratory for Green Chemical Technology of Ministry of Education, School of Chemical Engineering and Technology
Tianjin University
E-mail: jlgong@tju.edu.cn
Assoc. Prof. Dr. T. Wang, Prof. Dr. J. Gong
Collaborative Innovation Center of Chemical Science and Engineering
Tianjin 300072, P.R. China

advantages to the PEC activity. The bulk properties of single crystals can be finely controlled by the industrially mature processes such as the Czochralski growth. As the crystallinity, dopant concentration, carrier diffusion length are well-optimized with high reproducibility, the bulk recombination and carrier transportation become less of a problem. Thus, tailoring the surface properties and energetics of single-crystal semiconductors stands out as the particularly important and effective approach to improve the overall efficiency.

The costs of single-crystal substrates, especially for those containing rare elements and compounds such as InP, might be a concern, but the achieved high performance may partially trade off the costs.[9] These highly defined photoelectrodes could also serve as excellent models to understand the rate-limiting processes in PEC water splitting. Moreover, as the second most abundant element in Earth's crust, Si still dominates the solar cell market. The costs of single-crystal Si PEC electrodes can be largely reduced by transferring knowledge obtained from single crystals to electrodes of the same material but produced in a low-cost fabrication process using material-efficient configurations, such as solar-grade multicrystalline Si or thin films, which has already been adopted by the photovoltaics industry.[10]

A main obstacle to using narrow-band-gap semiconductor for water splitting is that these materials suffer from photocorrosion or passivation in contact with aqueous electrolytes, under either operation or idle conditions. Additionally, the sluggish water splitting kinetics on semiconductor surfaces is another major limiting factor. To generate a photovoltage higher than half of 1.23 V, which is required for overall water splitting for tandem water splitting cells, the surface energetics of narrow-band-gap semiconductors must be optimized. Lastly, a carefully controlled morphology of the photoelectrodes is desired for maximum antireflection and surface hydrophilicity.

This Minireview overviews the recent research progresses in surface monifications for single-crystal semiconductors with narrow band gaps for solar water splitting. First, strategies for surface protection are summarized. Second, surface cocatalysts for the HER and the OER are introduced. Construction of homo- and herterojuncions for surface energetics optimization is then discussed. Additionally, surface texturization methodes are briefly described.

## 2. Surface Protection

A fundamental problem shared by many narrow-band-gap semiconductors (Si, InP, GaAs, etc.) is their photocorrosion or passivation in aqueous electrolytes. This is especially true for n-type semiconductors with narrow band gaps that always have thermodynamic oxidation potentials above the $O_2/OH^-$ redox potential. For this type of semiconductors, self-oxidation reaction would compete with the water oxidation reaction, resulting in serious photocorrosion and the formation of insulating surface oxide layers. Even though this issue is less serious for p-type semiconductors under cathodic protection, surface oxidation is still a concern for photocathode under idle conditions or in alkaline electrolytes.[11] It was found that the dissolved $O_2$ concentration must be less than 15 ppb to prevent p-type Si from oxidation, which is unfeasible for practical applications.[12] One possible solution is to coat a surface protective layer while allowing sufficient interfacial transfer of photogenerated minority carriers.

### 2.1. Surface Protection for Photocathodes

#### 2.1.1. Ultrathin Tunneling Protective Layers for HER

Coating protective oxide layers that are thin enough to allow electrons to tunnel through are effective to both photocathodes and photoanodes. With a metallic overlayer acting as a surface catalyst or electron collector on top of the oxide layer, such electrode protection methodology is sometimes referred to as a metal–insulator–semiconductor (MIS) photoelectrode design.

Esposito et al. has investigated the $H_2$ evolution mechanism using p-Si-based discontinuous MIS photocathodes.[13] Metallic Pt/Ti collectors (20/30 nm thick and 500 μm in diameter) were deposited onto p-Si(100) covered by 2 nm rapid thermal oxidation (RTO)-grown $SiO_2$, in a square lattice with 850 μm spacing. It was found that $H_2$ bubbles could evolve on the $SiO_2$ surface outside the Pt/Ti collector, and a photocurrent could be generated when a 25 μm diameter laser (532 nm) beam was positioned far away from the collector edge. Based on photovoltaic and catalytic properties acquired by scanning electrochemical techniques,

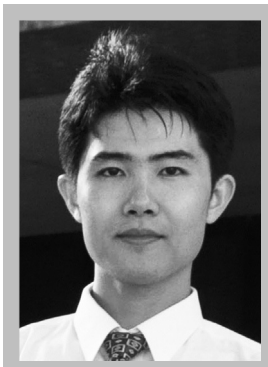

*Tuo Wang received his BS from Tianjin University and PhD (with Professor John G. Ekerdt) from the University of Texas at Austin, both in chemical engineering. After gaining another year of research experience as a postdoctoral associate, he joined Novellus Systems, Inc. (currently Lam Research Corp.) as a process development engineer in Tualatin, Oregon. Since August 2012, he has been an associate professor in chemical engineering in Tianjin University. His current research focuses on the fabrication of nanostructured and single-crystal materials for energy conversion and storage systems.*

*Jinlong Gong studied chemical engineering and received his B.S. and M.S. degrees from Tianjin University and his Ph.D. degree from the University of Texas at Austin under the guidance of C. B. Mullins. After a stint with Professor George M. Whitesides as a postdoctoral fellow at Harvard University, he joined the faculty of Tianjin University, where he currently holds a Pei Yang Professorship in chemical engineering. He was a visiting scientist at the Pacific Northwest National Laboratory in 2007. His research interests in catalysis include catalytic conversions of green energy, novel utilizations of carbon dioxide, and synthesis and applications of nanostructured materials.*

these phenomena could be explained by the long-distance lateral collection of photogenerated electrons through an electrolyte-induced inversion layer beneath the $Si/SiO_2$ interface, as well as the hydrogen spillover-assisted $H_2$ evolution on the $SiO_2$ surface.

More recently, the MIS PEC photocathode design was further thoroughly studied by Ji et al. using four-unit-cell (ca. 1.6 nm) molecular beam epitaxy (MBE)-grown $SrTiO_3$ as a corrosion-resistant layer on p-type Si(001) for $H_2$ production.[14] The negligible conduction-band offset between $SrTiO_3$ and Si could facilitate electrons to tunnel through. In addition, this MBE-grown $SrTiO_3$ is featured by its single-crystalline nature, a small lattice mismatch (−1.7%) with Si(001), as well as a high-quality $SrTiO_3$-Si epitaxial interface with reduced recombination centers. Covered by discontinuous metallic Pt/Ti (20/30 nm thick) cocatalyst with 1 μm diameter in a square array of 2 μm spacing, the p-Si/$SrTiO_3$/Ti/Pt MIS cathode exhibited an open circuit potential of 450 mV, and a saturate photocurrent density of 35 mA cm$^{-2}$, with no observable degradation after 35 h (Figure 1a) of operation at 0 V versus Ag/AgCl (0.5 M $H_2SO_4$, AM1.5G). The existence of an inversion layer underneath $SrTiO_3$ was confirmed by solid-state capacitance–voltage measurements, which supported the electron travelling mechanism proposed by Esposito et al.[13] The optimized Pt/Ti cocatalyst patterning with 0.05 μm diameter and 0.1 μm spacing using the nanosphere lithography lift-off process yielded a high energy conversion efficiency of 4.9%.

### 2.1.2. Thick $TiO_2$ Protective Layers for HER

Although ultrathin layers allow direct tunneling, thicker $TiO_2$ protective layers with efficient electron transfer cannot be explained by the same theory. Chorkendorff and coworkers carefully investigated the electron conducting mechanism of thick $TiO_2$.[15] $TiO_2$ (100 nm thick) was sputtered on top of a 5 nm Ti metal layer, which protected the underlying pn$^+$-Si(100) photocathode for $H_2$ evolution for 72 h. Interestingly, the pn$^+$-Si/Pt, pn$^+$-Si/Ti/Pt, and pn$^+$-Si/Ti/$TiO_2$/Pt electrodes displayed a similar HER onset potential of 0.52 V versus RHE (1 M $HClO_4$), and a similar Tafel slope of 30 mV dec$^{-1}$ under the long-wavelength part of AM1.5G irradiation ($\lambda > 635$ nm, the possible working spectrum of the cathode component of a tandem water splitting device), indicating that the 100 nm $TiO_2$ layer imposed negligible Ohmic resistance to the electrode; that is, $TiO_2$ behaves like a metallic conductor. The authors ascribed this behavior to the alignment of the $TiO_2$ conduction band with the $H^+/H_2$ redox potential, which allows the electrons from Si to easily travel through the $TiO_2$ layer. With optimized annealing conditions, the pn$^+$-Si/Ti (5 nm)/$TiO_2$ (100 nm)/Pt electrode exhibited an excellent HER photocurrent stability without significant degradation over 72 h (Figure 1b) at 0.3 V versus RHE (1 M $HClO_4$, AM1.5G with $\lambda > 635$ nm). The stability of a $TiO_2$-protected pn$^+$-Si photocathode can be further improved by using a 100 nm $TiO_2$ layer deposited by atomic layer deposition (ALD).[16] ALD has been recognized as an enabling thin-film deposition technique for PEC electrodes.[17] It was found that the ALD-grown $TiO_2$ was superior to sputtered $TiO_2$ in terms of stability, owing to the prevention of

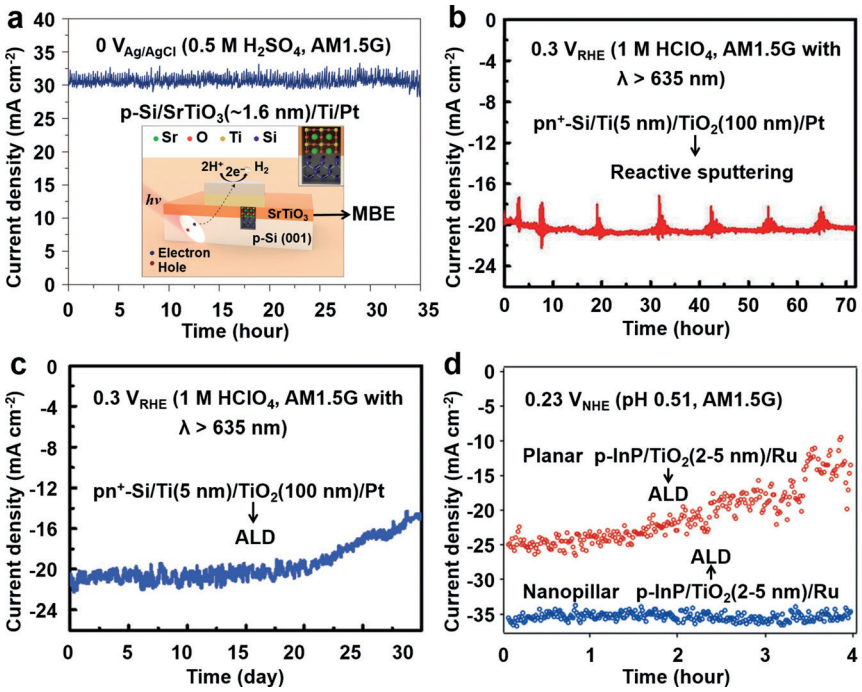


***Figure 1.*** Photocathodes with protective layers under HER conditions: a) p-Si protected by MBE-grown $SrTiO_3$ (four unit cells, 1.6 nm),[14] b) pn$^+$-Si protected by sputtered $TiO_2$ (100 nm),[15] c) pn$^+$-Si protected by ALD-grown $TiO_2$ (100 nm),[16] d) p-InP protected by ALD-grown $TiO_2$ (2–5 nm).[20] Reproduced with permissions. Copyright 2014 Nature Publishing Group. Copyright 2013 American Chemical Society. Copyright 2014 The Royal Society of Chemistry. Copyright 2012 Wiley-VCH.

a high deposition temperature and the bombardment of $TiO_2$ particles during the sputtering process. With optimized post-deposition annealing conditions of 400 °C for 1 hour, the ALD-$TiO_2$ protected $pn^+$-Si(100) electrode exhibited a remarkable stability over two weeks (Figure 1c), producing a stable photocurrent of 21 mA cm$^{-2}$ at 0.3 V versus RHE (1M $HClO_4$, AM1.5G with $\lambda > 635$ nm). As a cost-efficient alternative, a solution-deposited stack of 50 nm $TiO_2$ on top of 50 nm F:$SnO_2$ was also found to be able to protect a micro-textured $pn^+$-Si substrate in 1M KOH for $H_2$ evolution for 24 h.[18]

$TiO_2$ with the conduction-band electron-transport mechanism was also applied to protect amorphous Si based photocathodes. Javey and colleagues deposited 80 nm of $TiO_2$ using reactive sputtering on top of 8 nm sputtered Ti layer to protect amorphous Si PEC cathodes with Ni-Mo catalytic layer and buried p-i-n junction (Ni-Mo cocatalyst and p-i-n junction will be discussed in Section 3.1.3 and 4.1, respectively).[19] The thin Ti layer was introduced to prevent the damage of amorphous Si during the $TiO_2$ sputtering process. The resulting Si/Ti/$TiO_2$/Ni-Mo electrode showed a stable photocurrent of 11 mA cm$^{-2}$ at 0 V versus RHE (pH 4, AM1.5G), with less than 5% decay over 12 h. The amorphous Si photocathode without the $TiO_2$ protective layer decayed to 10% of its original photocurrent after 12 h.

The same group also disclosed the anti-corrosion ability of $TiO_2$ for p-InP photocathode.[20] InP nanopillars fabricated from p-InP(100) were protected by ALD-grown amorphous $TiO_2$ (2–5 nm) with a sputtered Ru cocatalyst (2 nm). The nanopillar p-InP/$TiO_2$/Ru electrode presented a stable HER photocurrent of 37 mA cm$^{-2}$ for more than 4 h (Figure 1d, black circles) at 0.23 V versus NHE in 1M $HClO_4$ (pH 0.51, 0.26 V vs. RHE) under AM1.5G, and the morphology of the electrode remained unchanged after the stability test according to scanning electron microscopy (SEM). A record high energy conversion efficiency of 14% was obtained at 0.5 V versus NHE (pH 0.51, 0.53 V vs. RHE) under AM1.5G. Furthermore, the authors explored the specific role of ALD-grown $TiO_2$ when protecting planar p-InP(100) substrates.[21] In addition to the anti-corrosion effect, 10 nm stoichiometric $TiO_2$ without $Ti^{3+}$ species could induce a 200 mV anodic shift for the water reduction onset potential without affecting the saturate photocurrent density. This additional photovoltage was caused by the type II heterojunction formed between InP and $TiO_2$, where the large valence band offset (1.9 eV) resulted in a large potential barrier for holes, repelling holes from the junction. As the conduction band of $TiO_2$ was well-aligned with that of InP, an electron transport pathway was established. With a 2 nm Pt catalytic layer, the planar p-InP/$TiO_2$/Pt photocathode exhibited an appreciable HER onset potential of 800 mV versus RHE (pH 0.3, AM1.5G), demonstrating the possibility of obtaining high photovoltage from anti-corrosion layers without fabricating buried p-n junctions.

### 2.2. Surface Protection for Photoanodes

Under water oxidation conditions, narrow-band-gap semiconductors are thermodynamically prone to self-oxidation, forming insulating oxides that block the transfer of photogenerated carriers. The photocurrent density of bare n-Si was essentially zero in strong alkaline solutions[22] or dropped to zero quickly during the second scan in neutral electrolytes.[23] Although transparent conductive oxides (TCOs) such as indium tin oxide (ITO) or fluorine-doped tin oxide (FTO) could protect the substrate against corrosion to some extent under neutral or mild pH conditions,[24] limited success with modified TCO has been reported for high pH solutions.[25] Ti films were also shown to enable Si to withstand the OER conditions or the oxidizing preparation procedures of cocatalyst, but the metallic nature of Ti makes it compete with the semiconductor for light absorption.[11b] Thus, robust and transparent protective layers are required to enable the n-type substrate to work under extreme pH conditions.

#### 2.2.1. Ultrathin Tunneling Protective Layers for OER

Although the oxidative environment is catastrophic to narrow-band-gap semiconductors, especially in base solutions, ultrathin oxides have been shown to be effective protective layers for continuous water oxidation operations. Chen et al. have demonstrated the successful protection of the n-type Si(100) photoanode under a wide pH range with a MIS design, by using an ALD-deposited $TiO_2$ layer (2 nm) with an e-beam-deposited Ir catalytic overlayer (3 nm).[26] The n-Si/$TiO_2$/Ir anode generated an appreciable photovoltage of 550 mV, and presented stable potentials in chronopotentiometric tests (constant 1 mA over a 0.196 cm$^2$ sample area) for more than 8 h under AM1.5G illumination under both 1M acid and 1M base conditions, while the anode without the 2 nm $TiO_2$ protective layer quickly failed within 0.5 h. The temperature independency of the $p^+$-Si/$TiO_2$ (2 nm)/Ir electrode in solid-state current–voltage measurements strongly indicated the direct tunneling mechanism for carrier transfer. The existence of the metallic overlayer was critical acting as a tunneling mediator for electron transport between the substrate and the solution.

Sharing a similar MIS PEC concept, Dai and colleagues demonstrated the protection of n-Si(100) using an ultrathin e-beam-deposited Ni film (2 nm), which was partially oxidized to form $NiO_x$ cocatalyst.[27] With the existence of Si native oxide, a MIS photoanode was formed and the n-Si/$SiO_2$/Ni/$NiO_x$ electrode exhibited a photovoltage of ca. 300 mV. When using a thicker 5 nm Ni film, acting as bulk nickel with relatively low work function (4.8–5.0 V[28]), the photovoltage produced by the MIS junction was decreased to ca. 200 mV. The higher effective work function of the ultrathin 2 nm Ni/$NiO_x$ resulted in a higher built-in potential at the MIS junction, which enabled a water oxidation onset potential of 1.07 V versus RHE, with a photocurrent density of 10.5 mA cm$^{-2}$ at 1.23 V versus RHE (pH 14, 2 Sun illumination). This Ni protected n-Si photoanode presented an impressively stable OER performance at 10 mA cm$^{-2}$ chronopotentiometric test for 80 h (Figure 2a) in a mixed lithium borate-potassium borate electrolyte (pH 9.5).

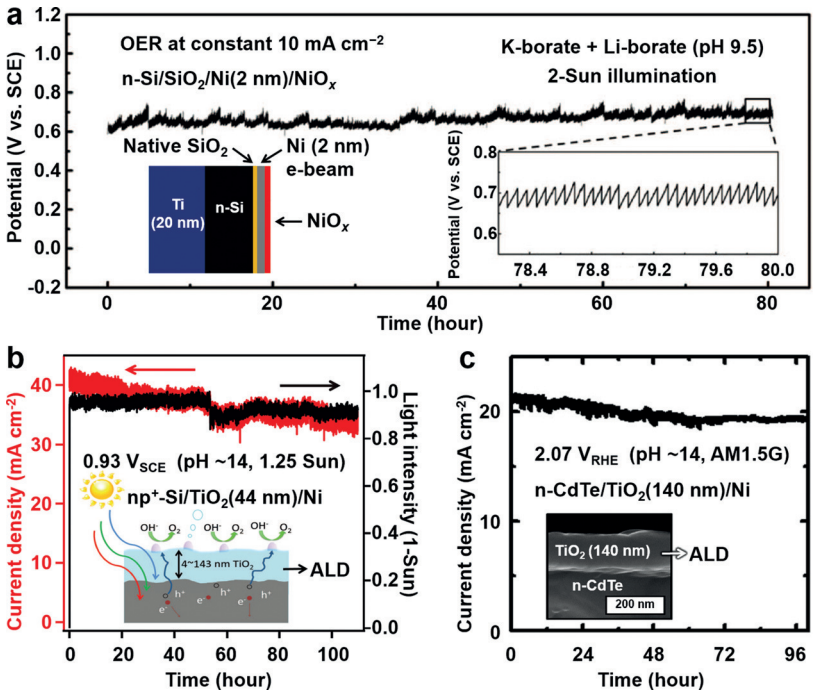


***Figure 2.*** Photoanodes with protective layers under OER conditions: a) n-Si protected by ultrathin e-beam-deposited Ni (2 nm),[27] b) $np^+$-Si protected by ALD-grown $TiO_2$ (44 nm),[28] c) n-CdTe protected by ALD-grown $TiO_2$ (144 nm).[30] Reproduced with permissions. Copyright 2013 AAAS. Copyright 2014 AAAS. Copyright 2014 The Royal Society of Chemistry.

### *2.2.2. Thick $TiO_2$ Protective Layers with Defect States for OER*

While electrons can easily inject into the conduction band of non-tunneling $TiO_2$ in p-Si-based photocathodes, thick $TiO_2$ films should present a potential barrier for holes owing to the large valence band offset (2.0 eV) between Si and $TiO_2$. Thus, it seems unlikely to use thick $TiO_2$ to protect photoanodes while allowing sufficient hole transport for water oxidation. However, Lewis and co-workers have elegantly demonstrated the successful protection of single-crystal Si, GaAs, and GaP photoanodes using ALD-grown amorphous $TiO_2$ (4 to 143 nm) that was electronically defective to promote hole conduction.[28] The existence of defect states were revealed by X-ray photoemission spectra, suggesting that holes could be transported through $TiO_2$ by the defect states instead of the valence band. These defect states were not presented in the topmost surface of as-deposited $TiO_2$, likely due to the oxidation by air or moisture. However, hole conduction pathways could be established by forming invasive contacts such as sputtering or e-beam evaporation of Ni cocatalysts that intermix with $TiO_2$ within a region of ca. 5 nm in depth, or physically removing the topmost layer of $TiO_2$. With ca. 100 nm Ni islands, the $np^+$-Si photoanodes protected by 44 nm $TiO_2$ maintained continuous OER operation of more than 100 h (Figure 2b) at photocurrent densities of more than 30 mA cm$^{-2}$ at 0.93 V versus saturated calomel electrode (SCE) (1M KOH, 1.25 Sun illumination, 2 V vs. RHE), with a Faradaic efficiency near unity. The fluctuations of the photocurrent were related to variations in the illumination intensity of the lamp. $np^+$-GaAs and n-GaP photoanodes protected by $TiO_2$ (118 nm) displayed photovoltages of 0.81 and 0.59 V, with saturate OER photocurrent densities of 14.3 and 3.4 mA cm$^{-2}$, respectively (1M KOH, AM1.5G).

This ALD-grown electronically defective $TiO_2$ can also be applied to protect II–VI semiconductors such as CdTe. With a direct band gap of 1.44 eV and large absorption coefficient of more than $10^4$ cm$^{-1}$, CdTe has found application in thin-film solar cells,[29] and exhibits potential for PEC solar water splitting. Like other narrow-band-gap semiconductors, however, CdTe suffers from photocorrosion. Amorphous ALD-deposited $TiO_2$ (140 nm thick) was found to effectively protect single-crystal n-CdTe(111) photoanodes against the corrosion or passivation in OER conditions.[30] A Ni layer (2 nm) was sputtered on top of $TiO_2$, which was further converted to a $NiO_x$ cocatalyst. The n-CdTe/$TiO_2$/Ni/$NiO_x$ photoanode showed a photovoltage of 435 mV with a saturate photocurrent density of 21 mA cm$^{-2}$ (pH 14, AM1.5G). This electrode also presented a stable OER photocurrent of 20 mA cm$^{-2}$ for more than 100 h of continuous operation (Figure 2c) at 2.07 V versus RHE (pH 14, AM1.5G), while the photocurrent of n-CdTe/Ni/$NiO_x$ electrode without $TiO_2$ decayed to 60% of its original value over 4 h under the same test condition.

While $TiO_2$ has been recognized as an effective protective layer for corrosion-vulnerable substrates, the hole conduction mechanism of thick $TiO_2$ (i.e., defect state-based) is fundamentally different from thin $TiO_2$ (tunneling) under water oxidation conditions,[26] as well as thick $TiO_2$ (electron transport by conduction band alignment) in water reduction conditions.[15]

### 2.3. Multifunctional Surface Protective Layers

Surface protective layers with multiple functions, such as serving as cocatalysts, are preferred. As a potential non-noble HER catalysts, $MoS_2$ was shown to protect $pn^+$-Si(100) photocathodes for water reduction over five consecutive days at 10 mA cm$^{-2}$ at 0 V versus RHE (1M $HClO_4$, AM1.5G with $\lambda > 635$ nm).[31] Angle-resolved X-ray photoelectron spectroscopy (XPS) revealed that the $MoS_2$ layer is unaffected after the stability test. This $MoS_2$ was prepared by thermal sulfidization of sputtered metallic Mo, which resulted in an inherently low concentration of active sites. Higher activity was obtained by loading the high-surface area electrodeposited $MoS_x$[11b] on top of $MoS_2$. This $MoS_2$ layer could effectively resist the oxidative condition of $MoS_x$ electrodeposition, and enabled the electrode to be reactivated for three 24-hour stability tests.

Sol–gel prepared crack-free catalytic $NiO_x$ films (37.4 nm thick) were able to protect n-type Si(100) under water oxidation conditions to some extent. The photocurrent density deceased from 6 to 1 mA cm$^{-2}$ at 1.3 V versus a Pt counter electrode during 4 h of intermittent operation over three days (pH 7.2, AM1.5G).[32] Crack-free catalytic $NiRuO_x$ films (ca. 20 nm) prepared by co-sputtering could also function as a protective layer for nanotextured n-Si(100) photoanode.[23] At 1.65 V versus RHE (pH 7.2, AM1.5G), the photocurrent density degraded from 7 to 5.95 mA cm$^{-2}$ after 500 cycles of pulsing external bias over 1.5 h, suggesting a relatively stable photoelectrode. Thinner ALD-deposited $CoO_x$ (4–5 nm) was also capable of protecting n-Si(100) from water oxidation, and the amorphous nature of the $CoO_x$ film was found to be critical to its anti-corrosion property.[33] When depositing on nanotextured $np^+$-Si, the amorphous $CoO_x$ with minimum grain boundaries could prevent the alkaline solution from attacking the substrate. The nanotextured $np^+$-Si/$CoO_x$ electrode presented a stable potential of 1.2 V versus RHE to maintain a constant 10 mA cm$^{-2}$, and exhibited a fairly stable photocurrent density of 2 mA cm$^{-2}$ at a constant bias of 1.1 V versus RHE (pH 13.6, AM1.5G) over 24 h, respectively.

Very recently, multifunctional $NiO_x$ protective coatings (70 nm) were also shown for a n-InP(001) substrate by Lewis and colleagues using reactive RF sputtering.[34] The $np^+$-InP/$NiO_x$ photoanode showed an OER onset potential of 0.86 V versus RHE, and a photocurrent density of 17.5 mA cm$^{-2}$ at 1.23 V versus RHE (1M KOH, AM1.5G). During the chronoamperometric test at constant 1.73 V versus RHE (1M KOH, AM1.5G), the photocurrent of the $np^+$-InP/$NiO_x$ electrode showed a 20% decrease during the first 2 h, and then remained constant at 20 mA cm$^{-2}$ for the remaining 46 h of operation, with a near unity Faradaic efficiency, indicating the excellent anti-corrosion ability of sputtered $NiO_x$ films. Moreover, the $NiO_x$ layer could act as a catalytic layer with high transparency (optical band gap 3.74 eV), as well as an antireflective layer due to the refractive index matching.

## 3. Surface Cocatalysts

One of the bottleneck issues for solar water splitting is the sluggish kinetics on semiconductor surfaces, which requires large overpotentials to drive the HER and the OER. Consequently, energy loss is significant during electron-transfer processes at the semiconductor/liquid interface. Cocatalysts could lower the activation energy or overpotential for $H_2$ and $O_2$ evolution reactions on the surface of semiconductors.[35] Pt are generally considered as the most effective HER cocatalyst, while $IrO_2$ and $RuO_2$ are well-known as excellent OER cocatalysts.[36] However, the scarcity and high costs of these noble-metal-based cocatalysts have hindered their application on a large scale. Thus, the design and development of non-noble water splitting cocatalysts with high efficiency is highly desired.[37]

### 3.1. HER Cocatalysts

Even though the HER is considered as an easier reaction compared to the OER, the $H_2$ evolution kinetics on p-type narrow-band-gap semiconductors is too sluggish to compete with the recombination of $e^-$-$h^+$ pairs.[38] Loading cocatalysts has been shown to be an efficient approach to solve this problem.

#### 3.1.1. Platinum-Group Metals as HER Cocatalysts

Pt-group metals are known as the best HER catalysts. Although they are rare and suffer from high cost, this group of metals may serve as archetypical catalysts to overcome the sluggish reaction kinetics, so that other performance-determining factors can be identified and optimized, such as the effectiveness of the anti-corrosion layer (using Pt,[15,16] Ir,[18] and Ru[20]), or the improvement of photovoltage from buried junctions (using Pt[11a]). Although highly catalytically active, the high work function of Pt (5.7 eV) should be considered when contacting with p-type semiconductors,[13] as discussed in Section 4.3.

#### 3.1.2. $MoS_x$ HER Cocatalysts

Using density functional theory (DFT) calculations, it has been predicted that the molybdenum edges of triangular $MoS_2$ nanoplatelets are highly electrochemically active for HER.[39] These surface-active sites were quantitatively identified by scanning tunneling microscopy (STM), and the HER catalytic activity of $MoS_2$ was verified by electrochemical measurements.[40] Based on these findings, Chorkendorff and colleagues further demonstrated that $Mo_3S_4$ can be an efficient HER catalyst for p-type Si(100) photocathode in strong acidic aqueous electrolyte (1M $HClO_4$) illuminated by AM1.5G irradiation with $\lambda > 620$ nm.[12] Upon the deposition of $Mo_3S_4$ clusters using a drop-casting method, the HER onset potential of a planar p-Si electrode was shifted from −0.4 to +0.15 V versus RHE (Figure 3a), exhibiting a hydrogen evolution current density of 8 mA cm$^{-2}$ at 0 V versus RHE. By forming a pillared structure with 2 nmol $Mo_3S_4$ loaded, the

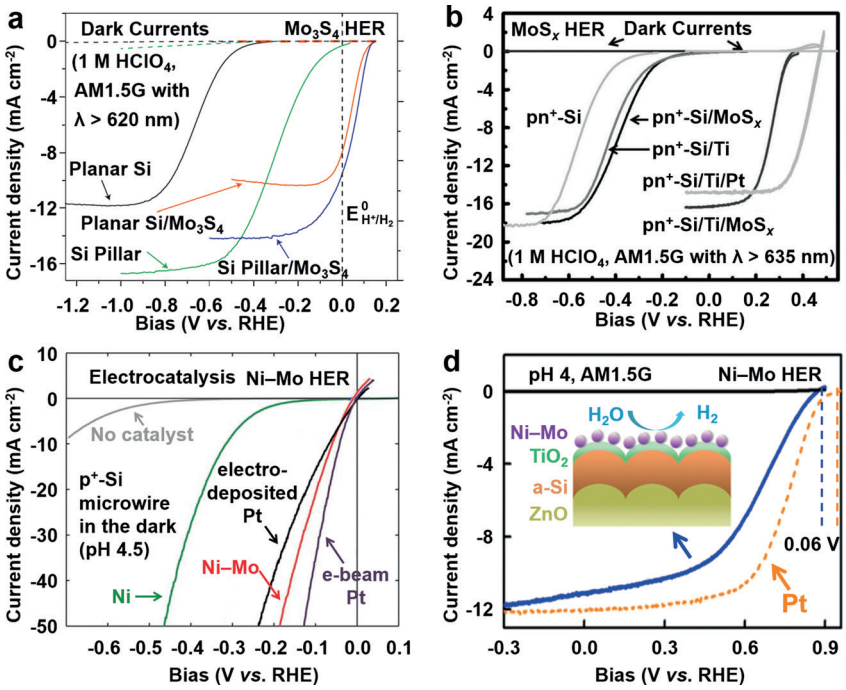


***Figure 3.*** HER catalytic effect of a) $Mo_3S_4$[12] and b) $MoS_x$[11b] with Si photocathodes under AM1.5G. c) HER electrocatalytic effect of Ni-Mo alloy with p$^+$-Si in the dark.[41] d) HER catalytic effect of Ni-Mo alloy with amorphous Si under AM1.5G.[19] Reproduced with permissions. Copyright 2011 Nature Publishing Group. Copyright 2012 Wiley-VCH. Copyright 2011 The Royal Society of Chemistry. Copyright 2013 American Chemical Society.

photocurrent density was further improved to 9 mA cm$^{-2}$ at 0 V versus RHE. High-surface area amorphous $MoS_x$ can also be electrodeposited onto pn$^+$-Si(100).[11b] To protect pn$^+$-Si against the oxidative condition during the $MoS_x$ electrodeposition process, a 9 nm Ti protective layer was sputtered first, which also prevented the Si(100) substrate from passivation by dissolved $O_2$ during the HER and under idle conditions. Upon the deposition of $MoS_x$, the pn$^+$-Si/Ti/$MoS_x$ electrode showed a substantial shift of HER onset potential (at 1 mA cm$^{-2}$) to 0.33 V versus RHE, as compared to the onset potential of −0.22 V versus RHE for pn$^+$-Si/Ti electrode (Figure 3b). This catalytic effect was comparable to that of Pt (0.47 V vs. RHE onset potential for pn$^+$-Si/Ti/Pt), while $MoS_x$ was less likely to block the light absorption, rendering a photocurrent density of 16.2 mA cm$^{-2}$ at 0 V versus RHE (1M $HClO_4$, AM1.5G with $\lambda > 635$ nm), higher than the Pt catalyzed electrode (14.8 mA cm$^{-2}$ at 0 V vs. RHE).

Improved photocatalytic HER performance was also observed for p-InP(111) decorated by $MoS_x$ nanoparticles using a photochemical reduction process.[5] Transmission electron microscopy (TEM) images revealed that the photochemical deposited $MoS_x$ was amorphous. XPS confirmed the composition of $MoS_3$. When $MoS_3$ was deposited on a planar single-crystal p-InP electrode, the open circuit voltage increased from 0.20 to 0.55 V versus RHE (1M $HClO_4$, AM1.5G), and the maximum energy conversion efficiency increased from 0.3 to 3.9%, primarily due to the catalytic effect of $MoS_3$, while the surface passivation effect of $MoS_3$ was also revealed by photoluminescence tests. For single-crystal p-InP with 3% of the surface covered by InP nanowires, depositing $MoS_3$ nanoparticles could improve the maximum energy conversion efficiency from 1.2 to 6.4%, which was among the highest efficiency reported for PEC water reduction using nanowire-based photocathodes. At 0 V versus RHE (1M $HClO_4$, AM1.5G), the $MoS_3$ decorated p-InP nanowire electrode was relatively stable with a photocurrent retaining 93% of its initial value after one hour.

### *3.1.3. Ni-Mo Alloy HER Cocatalyst*

Ni-Mo alloy HER catalysts were investigated by Lewis and colleagues as an earth-abundant alternative that may replace the noble metal catalysts. The Ni-Mo nanoparticles were electrodeposited from a bath containing Ni$^{II}$ sulfamate and $Na_2MoO_4$ at pH 4.5, onto p$^+$- and p-type Si,[41] as well as planar and microwire-array pn$^+$-junction Si.[42] The selection of an acidic Ni$^{II}$ sulfamate bath avoided the electrodeposition process under alkaline conditions that would oxidize the Si surface. For both planar and microwire-array p$^+$-Si electrodes in the dark (pH 4.5), the Ni-Mo alloy exhibited considerably higher dark electrocatalytic activity than electrodeposited Ni nanoparticles, primarily due to the improved surface area. The electrocatalytic activity of Ni-Mo alloy nanoparticles was comparable to e-beam-deposited Pt film (ca. 1 nm) and higher than electrodeposited Pt nanoparticles for p$^+$-Si microwire samples (Figure 3c). Despite the noticeable catalytic activity of the Ni-Mo alloy in the dark, no substantial improvement of HER onset potential was observed for the p-Si/Ni-Mo electrode under AM1.5G illumination (pH 4.5), which was ascribed to the lower photovoltage generated by

the p-Si/Ni-Mo interface due to the less effective "pinch-off" effect (more discussions in Section 4.3).[41] In the case of $pn^+$-Si where the photovoltage was generated from the buried $pn^+$ junction, the $pn^+$-Si/Ni-Mo microwire-array photocathode yielded an energy conversion efficiency of 1.9% under AM1.5G illumination (pH 4.5).[42] Javey and co-workers also electrodeposited this Ni-Mo catalyst onto $TiO_2$ protected p-i-n amorphous Si photocathodes.[19] The Ni-Mo catalyzed amorphous Si electrode showed an onset potential of 0.87 V versus RHE, only 0.06 V more negative than that of a reference electrode catalyzed by a 2 nm Pt film (Figure 3d), under AM1.5G illumination (pH 4), indicating the high HER catalytic activity of this Ni-Mo alloy.

### 3.2. OER Cocatalysts

Being the first step of water splitting, the OER is particularly demanding due to its intrinsic nature as an energy uphill reaction that involves a four-electron oxidation of two water molecules, leading to the removal of four protons to form an O-O double bond. Subsequently, the four protons and four electrons released from OER could be combined to form two hydrogen molecules in the HER half reaction.[43] The activation energy of water oxidation dominates that of the overall water splitting reaction.[44] Most of the photovoltage produced by the photoanode is used to overcome the sluggish $O_2$ evolution kinetics coupled with rapid charge recombination. Thus, efficient water oxidation cocataysts are expected to improve the efficiency of water splitting significantly.

#### 3.2.1. Noble Metals as OER Cocatalysts

An $Ir/IrO_x$ film stack was prepared by sputtering as an OER catalyst for $np^+$-Si photoanodes in an acidic media (1M $H_2SO_4$). Upon thermal treatment at 648 K, the $np^+$-Si/$Ir/IrO_x$ electrode exhibited a photocurrent density of 10 mA cm$^{-2}$ at 1.23 V versus RHE under AM1.5G irradiation with $\lambda >$ 635 nm. Without inserting an extra interfacial anti-corrosion layer, this 2 nm $Ir/IrO_x$ catalytic layer could protect the Si substrate against corrosion for 18 h at 1.23 V versus RHE.[45] The high activity of $IrO_x$ is not unexpected, but it is still highly desirable to enable earth abundant materials to replace, or at least diminish the usage of noble metals.

A $NiRuO_x$ catalytic film was synthesized by RF co-sputtering using NiO and Ru targets on a n-type Si(100) photoanode.[23] Upon the incorporation of $RuO_x$, the $Ni^{II}/Ni^{III}$ ratio changed from 0.86 to 0.35 as revealed by XPS, indicating that the $NiRuO_x$ film was $Ni^{III}$-rich. By depositing this $NiRuO_x$ film on FTO, the dark OER overpotentials at 10 mA cm$^{-2}$ decreased from 1829 (bare FTO) to 797 mV versus RHE (pH 7.2), which outperformed the pure $NiO_x$ film that needed a 1043 mV overpotential to drive the same current density. For the n-Si/$NiRuO_x$ photoanode under AM1.5G illumination, an onset potential of 1.08 V versus RHE (pH 7.2) was observed, with a photocurrent density of 0.94 mA cm$^{-2}$ at 1.23 V versus RHE. This PEC water oxidation performance is comparable to an n-Si(100) photoanode directly coated with metallic Ru (n-Si/Ru) with similar Ru loading.

#### 3.2.2. Cobalt-Phosphate (Co-$P_i$) OER Cocatalysts

Nocera and colleagues pioneered the in situ formation of a Co-based OER cocatalyst on conductive electrodes by the electrodeposition of $Co^{2+}$ ions in aqueous solutions containing phosphate at pH 7 (denoted as Co-$P_i$). The resulting Co-$P_i$ catalytic thin film was amorphous with a Co to phosphate ratio of about 2:1.[46] Co-$P_i$ catalytic films can also be prepared directly from 800 nm thick cobalt metal thin films on non-conductive Si substrates in phosphate-containing solutions at pH 7, where the metallic cobalt partially transformed into Co-$P_i$ while the remaining cobalt metal could act as the protective layer.[47]

Using the solution-based method with potassium phosphate and $Co^{2+}$, the Co-$P_i$ film was deposited on $npp^+$-Si, with a conductive ITO layer sandwiched between Co-$P_i$ and Si as the protective layer. The electrode exhibited an onset potential of 0.7 V versus NHE at pH 7 (1.1 V vs. RHE) under AM1.5G illumination, producing a photovoltage of 0.52 V.[24a] Using a triple junction (3jn) amorphous Si solar cell covered with ITO as the anode, the solution-deposited Co-$P_i$ catalytic layer resulted in an negative onset potential of −0.37 V versus RHE (1M potassium borate, pH 9.2, AM1.5G) for water oxidation, which enabled spontaneous water splitting using NiMoZn on Ni mesh as the counter electrode with an overall efficiency of 4.7% (Figure 4a).[24b]

#### 3.2.3. 3d Metal (Ni, Co, Fe, Mn) Oxides as OER Cocatalysts

3d Transition-metal (Ni, Co, Fe, Mn) oxides have been demonstrated as promising earth-abundant OER cocatalysts, and an amorphous $Fe_{(100-y-z)}Co_yNi_zO_x$ composite prepared by a photochemical deposition method presented comparable activity to noble-metal oxide catalysts.[48] Another cost-effective sol–gel process followed by drop casting was presented by Wang and co-workers to prepare crack-free $NiO_x$ films (37.4 nm thick) on n-type Si(100).[32] Upon annealing at 400°C for improved crystallinity, the sol–gel $NiO_x$ film became oxygen rich with $Ni^{2+}$ being the dominant nickel species. Although the number of $Ni^{3+}$, which was the OER catalytic centers, reduced upon annealing, the $NiO_x$ film still exhibited noticeable catalytic effect for water oxidation, since the onset potential (at 0.1 mA cm$^{-2}$) of n-Si/ITO/$NiO_x$ showed a significant cathodic shift (ca. 900 mV) compared to an n-Si/ITO electrode (Figure 4b) under AM1.5G illumination at pH 7.2, resulting in an overall conversion efficiency of 1.34%. Furthermore, a porous $NiO_x$ OER catalyst was synthesized by adding a non-ionic surfactant as the complexing agent in the precursor, which produced dense and compact $NiO_x$ nanoparticles, providing a large surface area, and the catalyst activation processes could be simplified.[25]

$CoO_x$ catalytic layers deposited by plasma-enhanced ALD from $Co(Cp)_2$ and $O_2$ plasma was demonstrated by Sharp and colleagues to assist the water oxidation on nano-textured $np^+$-Si buried junction substrate.[33] The $np^+$-Si/$CoO_x$ electrode exhibited a photocurrent density of 17 mA cm$^{-2}$ at

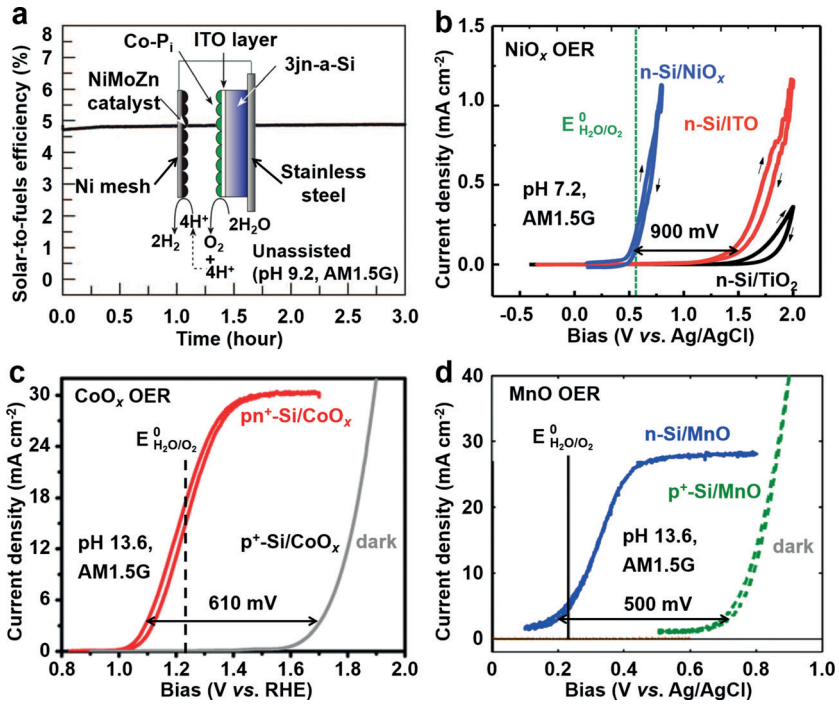


***Figure 4.*** a) Unassisted solar water splitting with Co-P$_i$ as the OER cocatalyst, resulting in an energy conversion efficiency of 4.7%.[24b] OER catalytic effect of b) $NiO_x$,[32] c) $CoO_x$,[33] and d) MnO[22] with Si photoanodes. Reproduced with permissions. Copyright 2011 AAAS. Copyright 2012 The Royal Society of Chemistry. Copyright 2014 American Chemical Society. Copyright 2013 American Chemical Society.

1.23 V versus RHE (pH 13.6, AM1.5G) (Figure 4c). XPS and X-ray absorption near-edge spectroscopy (XANES) indicated that these $CoO_x$ films are composed of $Co_3O_4$ with an underlying interfacial $Co^{II}$ layer. Surface CoO(OH) species were formed upon water oxidation reaction for one hour.

Jacobson and co-workers deposited Ti-doped α-$Fe_2O_3$ (Ti:$Fe_2O_3$) films on n-type Si(100) as the catalytic layer.[49] The ultrathin (< 10 nm) $Fe_2O_3$ permitted the space charge region to be primarily within silicon, which enabled silicon to preserve its upward band bending at the semiconductor–liquid junction without being disturbed by the Ti:$Fe_2O_3$ catalytic layer. The Ti:$Fe_2O_3$ catalyzed planar n-Si photoanode with optimized cocatalyst thickness and backside contact displayed an onset potential of 1.05 V versus RHE, and reached photocurrent density of 12 mA cm$^{-2}$ at 1.23 V versus RHE (pH 13.8, AM1.5G).

Additionally, a MnO thin film (10 nm) was deposited on n-type Si(100) by ALD. While bare n-Si exhibited negligible photocurrent, n-Si/MnO presented an ORE current density of 4.5 mA cm$^{-2}$ at 1.23 V versus RHE, and a saturate value of 28 mA cm$^{-2}$ (1M KOH, AM1.5G) (Figure 4d). With p$^+$-Si/MnO in the dark as reference, the n-Si/MnO electrode produced a high photovoltage of ca. 500 mV, indicating the OER catalytic effect of MnO.[22]

## 4. Surface and Interface Energetics

### 4.1. Buried Junctions for Higher Photovoltage and Device Flexibility

Another limitation of narrow-band-gap semiconductor photoelectrodes is the relatively small photovoltage as compared to other semiconductors such as $TiO_2$, owing to their intrinsic small band gap and unfavorable band positions. Lewis and colleagues investigated the hydrogen evolution ability of Pt decorated planar (100)-oriented and microwire-array p-Si electrodes.[11a] Although a highly active Pt electrocatalyst was used, it was found that the performance was still low for both planar (Figure 5a) and microwire-array (data not shown) p-Si/Pt electrodes, primarily due to the small photovoltage produced at the p-Si/solution junction, since the valence band edge energy of Si is not positive enough with respect to the $H^+/H_2$ redox potential (Figure 5c), consistent with the previous finding.[38] In addition, the p-Si/Pt Schottky junction was also incapable of generating a significant built-in potential owing to the limited difference between the work function of p-Si and Pt.[13,14] (more details in Section 4.3).

To obtain a higher photovoltage, a top n$^+$ emitter layer was introduced to form a buried pn$^+$ junction as in photovoltaic solar cells, using the thermal diffusion method.[11a] Upon the formation of buried pn$^+$ junction, the generation of photovoltage is decoupled from the semiconductor/solution interface where the electrocatalyst is loaded (Figure 5d). Thus, the Schottky junction at the semiconductor/solution interface is no longer required, which allowed the surface cocatalysts to be optimized independently. In addition, edge

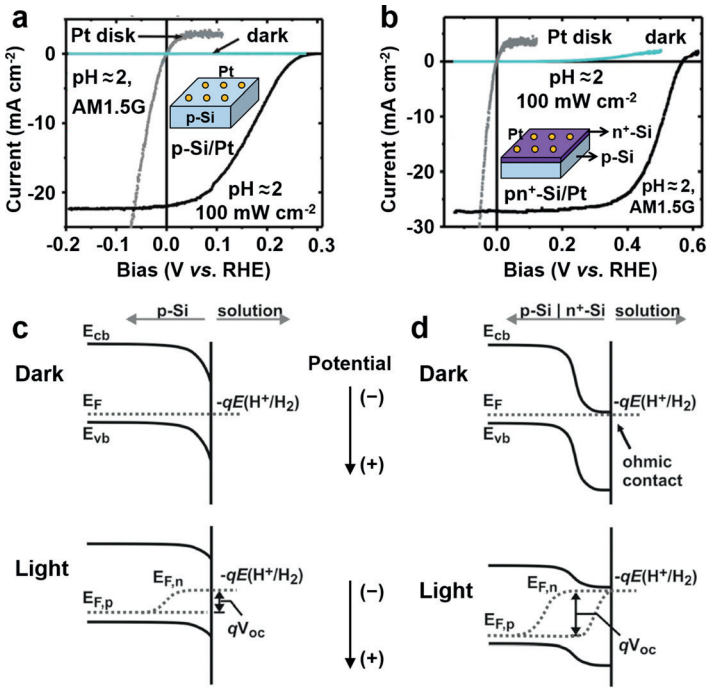


***Figure 5.*** Increased photovoltage by forming buried p-n junctions. Photocurrent density-potential behaviors of a) planar p-Si/Pt and b) planar $pn^+$-Si/Pt photocathodes, where the top $n^+$ emitter layer induces a higher photovoltage (0.55 V compared to 0.3 V). Band diagrams of c) p-Si and d) $pn^+$-Si photocathodes in the dark and under illumination, in contact with the $H^+/H_2$ redox couple in solution. The photovoltage ($V_{oc}$) of $pn^+$-Si is larger because of the increased band bending at the $p/n^+$ junction relative to the p-Si/solution junction.[11a] The ultrathin upward band bending at the $n^+$-Si/solution interface is omitted for clarity purpose. Reproduced with permission. Copyright 2011 American Chemical Society.

positions of the conduction and valence band are not required to be more negative or positive than the thermodynamic HER or OER redox potentials, respectively, as long as the photovoltaic cell could provide enough potential for water splitting.[24c]

A shallow upward band bending (not shown in Figure 5d for clarity) exists at the $pn^+$-Si/solution interface, but the depth of this band bending is limited to a few nanometers owing to the high doping level in the $n^+$ layer, thus the minority carriers (holes for photocathodes) can easily tunnel through. This is the reason why a shallow and heavily doped top $n^+$ layer is preferred for p-type substrates.

The resulting planar (Figure 5b) and microwire-array (data not shown) $pn^+$-Si/Pt electrodes both exhibited stable and reproducible photovoltages of 0.55 V, with energy conversion efficiencies of 9.6 and 5.8%, respectively (pH 2, AM1.5G), which is among the highest for Si-based photocathode. By using a textured commercial $pn^+$-Si substrate coated with $F:SnO_2/TiO_2$ as the anti-corrosion layer and an Ir cocatalyst (2 nm thick), the textured $pn^+$-Si photocathode reached an energy conversion efficiency of 10.9% (1M KOH, AM1.5G).[18] Similar planar[11b] and microwire-based[42] p-type Si with top $n^+$ emitter layers were also used to fabricate high-performance photocathodes by loading $MoS_x$ and Ni-Mo alloy cocatalysts.

Forming buried homogenous p-n junctions also allows n-type substrates to obtain increased photovoltages for water oxidation. A $np^+$-Si substrate has been fabricated using diffusion or ion implantation methods.[24a,25,33] A degenerately doped $p^+$-Si(100) electrode with MnO cocatalysts showed a dark OER onset potentials of 0.6 V versus Ag/AgCl (Figure 4d), corresponding to 1.6 V versus RHE at pH 13.6, very similar to $p^+$-Si(100) catalyzed by $CoO_x$ under similar test condition (Figure 4c), suggesting similar activity of the two cocatalysts prepared by the two groups. Under AM1.5G illumination, the $np^+$-Si(100)/$CoO_x$ electrode produced a photovoltage of 610 mV,[33] while the n-Si(100)/MnO photoanodes only produced ca. 500 mV.[22] This is largely due to the difference between the metallurgic $np^+$ junction and the n-Si/solution junction.

In addition to the metallurgical p-n junctions constructed within Czochralski-grown Si substrates by dopant diffusion or ion implantation, buried junctions can also be fabricated using bottom-up techniques such as thin-film deposition. A $p^+$-doped emitter layer (100 nm) was deposited on n-type single-crystal InP(001) substrates using gas-source MBE, and the $np^+$-InP anode generated a photovoltage of 700 mV for water oxidation.[34] Javey and co-workers demonstrated the fabrication of amorphous Si with buried p-i-n junction using plasma enhanced CVD (PECVD).[19] Covered by a $TiO_2$ protective layer and a Pt catalytic layer, the p-i-n junction cathode exhibited an exceptionally positive HER onset potential of 0.93 V versus RHE, with a saturation photocurrent of 11.6 mA cm$^{-2}$, and reached an energy conversion efficiency of 6% for water reduction (pH 4, AM1.5G). Noticeably, the p-i-n junction cathode presented a sharp onset of photocurrent, and reached high values of 6.1 and 9.4 mA cm$^{-2}$ at large positive biases of 0.8 and 0.7 V versus RHE, respectively, which is the key to reach a high overall efficiency in a tandem PEC device where two half cells are

  

connected in series.[2] Very recently, Wang and colleagues fabricated a Si-based heterojunction structure with n-type single-crystal Si(001) sandwiched between PECVD-grown p-type amorphous Si (6 nm) and $n^+$-type amorphous Si (10 nm) layers, with ultrathin intrinsic amorphous Si presented at the two interfaces for dangling band passivation.[50] Generating a high open circuit voltage of 670 mV, this heterojunction device can be used as both photoanode and photocathode with ITO layers deposited to isolate Si from the electrolyte. Catalyzed by sol–gel-prepared $NiO_x$, the heterojunction photoanode with micropyramidal surface exhibited an OER photocurrent density of 10 mA cm$^{-2}$ at 1.06 V versus RHE, and an energy conversion efficiency of 1.5% (1M NaOH, AM1.5G). When loading Pt as the HER cocatalyst, this heterojunction photocathode presented a record high efficiency of 13.26% for water reduction with Si-based electrodes (1M $H_2SO_4$, AM1.5G). These examples clearly demonstrate the importance of buried junction in the enhancement of PEC water splitting efficiency.

### 4.2. Reduction of Interfacial Electrical Resistance

In addition to generating higher photovoltages, reducing the voltage drop due to resistive losses, and preventing the oxidation of the substrate or protective layers are also important considerations to ensure that all photovoltages are used to split water. For example, the backside of an n-Si(100) photoanode can be converted to a shallow $n^+$ layer by thermal diffusion to make Ohmic contact with the metallic aluminum/silver contact. With 10 nm $Fe_2O_3$ films as the cocatalysts for n-Si in 1M KOH (pH 13.8) under AM1.5G, the photocurrent density was significantly improved from 1.6 to 12.2 mA cm$^{-2}$ at 1.23 V versus RHE upon the formation of the $n^+$ back contact layer (Figure 6a,b).[49] To obtain more information about the Si/cocatalyst interface, Nocera and colleagues designed an npp$^+$-Si-based electrode configuration that can be used for OER to investigate the interfacial electrical resistances across the interfaces of the Si/protection-layer/cocatalyst structure, where the protective layer was conductive FTO, ITO, or Ni metal (Figure 6c).[24c] In semiconductor/solution junction-based photoelectrodes, p-Si is only suitable for water reduction. But for the npp$^+$-Si electrode with a buried junction where the np side is illuminated to generate photovoltage, the water oxidation reaction can take place on the unilluminated $p^+$ side, where different conductive protective layers and OER cocatalysts could be loaded to explore the interfacial voltage drop. In addition to not containing rare element indium, FTO was identified as a preferred interfacial protective layer compared to ITO and Ni, since FTO exhibited the best Tafel behavior among the three materials, with a 100% Faradic efficiency. When using Ni metal as the protective layer, about 80% Faradaic efficiency indicated the partial oxidation of Ni to $NiO_x$, suggesting that interfacial properties must be carefully controlled.

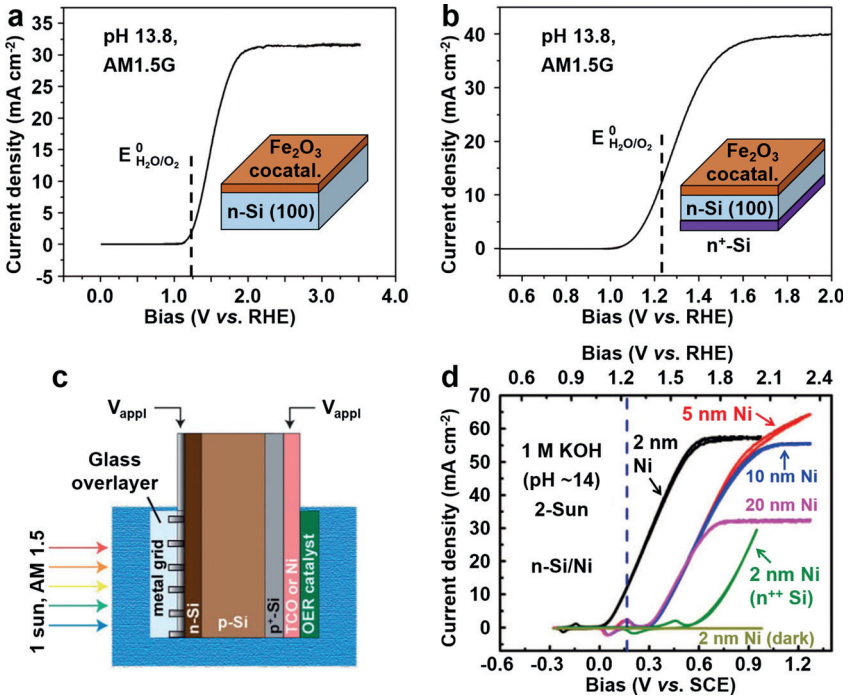


***Figure 6.*** Photocurrent density-potential behaviors of a) planar n-Si/$Fe_2O_3$ and b) planar $n^+$n-Si/$Fe_2O_3$ photocathodes, where the $n^+$ back contact layer significantly reduces the OER onset potential by forming Ohmic contact.[49] c) Schematic of the npp$^+$-Si buried-junction photoelectrode to investigate the interfacial voltage drop. Photoelectrocatalytic activity can be drawn by applying potential to the metal grid. When potential is applied to the TCO or Ni layer, results only reflect the activity of the OER catalyst.[24c] d) Higher photovoltage and lower onset potential obtained with n-Si(100) covered by ultrathin (2 nm) Ni metal with higher effective work function, in comparison with n-Si(100) covered by thicker (5, 10 and 20 nm) Ni films with relatively low work function.[27] Reproduced with permissions. Copyright 2012 Wiley-VCH. Copyright 2013 The Royal Society of Chemistry. Copyright 2013 AAAS.

### 4.3. Surface Energetics of Overlayers

Surface energetics also need to be considered when choosing overlayers for the substrate, such as cocatalyst layers or protective layers. Generally, when the overylayer is metallic, a low work function material is preferred for p-type substrate, while a high work function material is desired for n-type substrate. The Fermi level pinning at the interface is also a consideration.

Despite the excellent reaction kinetics enabled by Pt, the band bending at the Pt/semiconductor interface must be considered for photovoltage generation. The metallic electrocatalysts are preferred to form a Schottky junction with the underlying semiconductor, with a large work function difference, to facilitate the injection of photoinduced minority carriers to the metallic catalyst. Although Pt is an excellent HER catalyst, its work function is high (5.7 eV[13]) and similar to that of p-Si(5.0–5.2 eV[24a]), which may result in a small photovoltage.[13] By inserting a low work function metal, such as Ti (4.3 eV), between Pt and the p-Si(100) substrate, the photovoltage can be effectively improved.[13,14] These findings are consistent with the early investigation that p-Si(111) modified with Pt nanoparticles showed improved HER catalytic effect, but the photovoltage output was hampered.[38] A profound review with more details about metal/semiconductor interfacial energetics can be found elsewhere.[51]

Additionally, the work function of protective layer can be controlled to lower the barrier height for hole transport in n-type anodes. An investigation tuning the work function of the ITO (4.4–4.7 eV[24a]) protective layer for n-Si photoanode was recently reported by Wang and co-workers.[25] As a high work function metal, Au was sandwiched into ITO to increase its work function, which could facilitate the hole injection while retaining the transmittance of ITO. With modified work function, the ITO/Au/ITO layer was also an effective anticorrosion layer for the underlying $np^+$-Si substrate as relatively small water oxidation current decay was observed after 360 scans up to 0.9 V versus NHE (pH 13.8, 1.7 V versus RHE) under 0.51 Sun illumination. Similarly, n-Si(100) photoanode protected by ultrathin (2 nm) Ni metal generated a higher photovoltage and exhibited lower onset potential than those covered by thicker (5, 10, and 20 nm) Ni films (Figure 6d), due to the higher effective work function of ultrathin Ni relative to bulk Ni films. When the same 2 nm thick Ni films were deposited on top of other metals with different work functions to protect n-Si(100), the OER onset potential followed the order of n-Si/Ni(2 nm) < n-Si/Pt-(2 nm)/Ni(2 nm) < n-Si/Ti(2 nm)/Ni(2 nm). The inferior performance of n-Si/Ti(2 nm)/Ni(2 nm) was due to the low work function of Ti (4.3 eV[13]), resulting in a nearly Ohmic contact instead of a Schottky junction at the interface.[27]

The existence of continuous overlayers may also induce a high density of interface states, resulting in Fermi level pinning at the interface with decreased photovoltage generation. Instead, if discrete metallic particles are in contact with the semiconductor, the photovoltage will be primarily determined by the semiconductor/solution junction, rather than the semiconductor/metal junction, known as the "pinch-off" effect.[2] To ensure an effective "pinch-off" effect, the size of the particles should be comparable to the depletion width of the semiconductor, and these particles should be widely separated from each other. When Ni-Mo alloy nanoparticles were electrodeposited onto p-Si(100), the small interparticle distances and the intimate contact with Si surface resulted in a less prominent "pinch-off" effect. Thus, the photovoltage of p-Si/Ni-Mo was largely reduced.[41]

## 5. Surface Texturization

Like in many other semiconductor solar-to-fuel systems, nanotextured surfaces could provide an enlarged solid–liquid space charge layer area, and decouple the direction of light absorption from the direction of minority carrier transport.[52] For polished single-crystal planar substrates, surface texturization may provide additional advantages such as improved antireflection and surface wettability to facility the release of gas bubbles.

The polished planar single-crystal Si(100) substrates exhibited high specular reflectance of 55, 42, and 37% at ultraviolet (below 400 nm), visible (400 to 700 nm) and infrared (700 to 1100 nm) regions, respectively, at 30° incident angle. Upon surface nanotexturing using a chemical etching method, a broadband suppression of reflection was observed with a minimum value of ca. 0.1% at 640 nm (Figure 7a), accompanied by a 50% increase of OER photocurrent at 12.3 V versus RHE in a neutral electrolyte (pH 7.2) under AM1.5G (Figure 7b).[23] For water reduction, photolithographically prepared Si micropillars also showed enhanced HER photocurrent density from 8 to 9 mA cm$^{-2}$ at 0 V versus RHE (1M $HClO_4$, AM1.5G with $\lambda > 635$ nm) compared to planar p-Si(100) electrodes.[12] Similarly, both InP nanopillars (Figure 7c)[20] and InP nanowire arrays (Figure 7d)[5] were demonstrated to suppress the reflectance of polished planar InP from ca. 30 to 1% at 400 to 800 nm. A micropyramidal surface structure was also used to improve the light trapping of heterojunction Si substrates.[50] The antireflection ability of these patterned substrates was originated from the subwavelength surface micro- and nanostructures that can be considered as a mixture of the semiconductor and air, with gradient refractive index from air to substrate, serving as an antireflective layer.[53] Thus, nanoscale pyramid- or cone-like structures with shrinking lateral dimensions are preferred over nanorods or nanowires for antireflection purposes.

Fluctuating photocurrents with spikes were observed on planar Si(100) photoanodes due to the accumulation of $O_2$ bubbles on the electrode surface follow by rapid detachment (Figure 8a).[22] Similar $H_2$ bubble accumulation was also observed on planar InP(100) photocathodes, hindering the mass transportation between the electrolyte and the semiconductor, and reducing the electrode stability (Figure 1d, gray circles). These bubble accumulation issues were attributed to the hydrophobic nature of the planar semiconductors, which makes gases, instead of the electrolyte, stick to the surface. Upon the formation of an InP nanopillar structure (Figure 8b), the surface wettability of InP increased significantly as the contact angle of the electrolyte droplets decreased from 57 to 0° (Figure 8c,d), which significantly

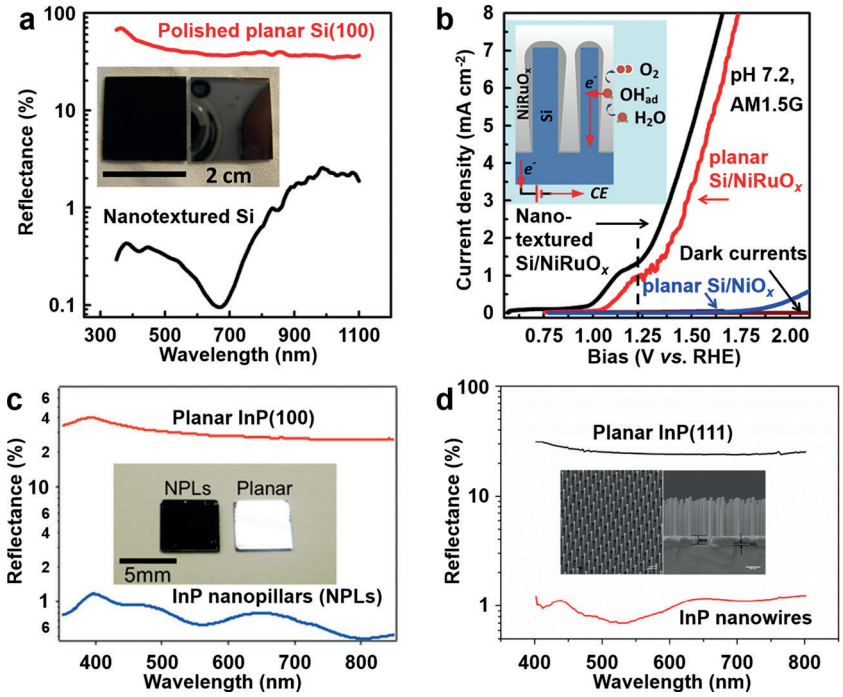


***Figure 7.*** a) Antireflection effect and b) improved photocorrent density of nanotextured Si, compared with planar Si samples.[23] Antireflection effects of c) InP nanopillars[20] and d) InP nanowire arrays,[5] compared with planar InP samples. Reproduced with permissions. Copyright 2013 American Chemical Society. Copyright 2012 Wiley-VCH. Copyright 2014 American Chemical Society.

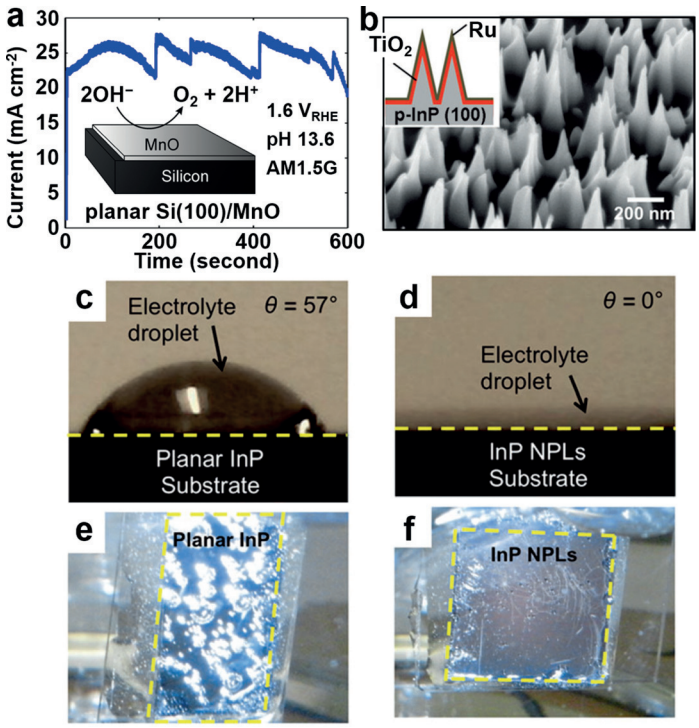


***Figure 8.*** a) Fluctuated photocurrents with spikes on planar Si(100)/MnO photoanodes caused by the accumulation of $O_2$ bubbles.[22] b) Morphology of surface textured InP nanopillar. c,d) Improved surface hydrophilicity and e,f) suppressed $H_2$ bubble accumulation upon the formation of InP nanopillar (NPL) photocathodes. Reproduced with permissions. Copyright 2013 American Chemical Society. Copyright 2012 Wiley-VCH.

suppressed $H_2$ bubble accumulation (Figure 8e,f). The InP nanopillar sample could further reduce the HER overpotential owing to a more intimate semiconductor/electrolyte interface.[20] Substrate surface texturization does not guaran-

***Table 1:*** Energy conversion efficiencies of recent representative PEC photoelectrodes based on narrow-band-gap semiconductors.

| Efficiency | Structure | Configuration | Conditions | Ref. |
|---|---|---|---|---|
| **HER** | | | | |
| 14% | p-InP/$TiO_2$/Ru | nanopillar | 1 M $HClO_4$ (pH 0.51), AM1.5G | [20] |
| 13.26% | Pt/ITO/($n^+$-i a-Si)/n-Si/(i-p a-Si)/ITO[a] | micropyramid | 1 M $H_2SO_4$, AM1.5G | [50] |
| 10.9% | $pn^+$-Si/F:$SnO_2$/$TiO_2$/Ir | micropyramid | 1 M KOH, AM1.5G | [18] |
| 9.6% | $pn^+$-Si/Pt | planar | 0.5 M $K_2SO_4$ (pH 2), AM1.5G | [11a] |
| 6.4% | p-InP/$MoS_3$ | nanowire | 1 M $HClO_4$, AM1.5G | [5] |
| 6% | p-i-n a-Si/$TiO_2$/Pt | deposited on textured ZnO | 0.5 M KHP[b] (pH 4), AM1.5G | [19] |
| 4.9% | p-Si/$SrTiO_3$/Ti/Pt | planar | 0.5 M $H_2SO_4$, AM 1.5G | [14] |
| **OER** | | | | |
| 4.7% | 3jn-a-Si/ITO/Co-Pi | deposited on stainless steel | 1 M KBi(pH 9.2), AM1.5G[c] | [24b] |
| 1.9% | $np^+$-Si/Ni-Mo | microwire | buffered KHP (pH 4.5),AM1.5G | [42] |
| 1.5% | ITO/($n^+$-i a-Si)/n-Si/(i-p a-Si)/ITO/$NiO_x$ | micropyramid | 1 M NaOH, AM1.5G | [50] |
| 1.34% | n-Si/ITO/$NiO_x$ | planar | buffered $Na_2SO_4$ (pH 7.2), AM1.5G | [32] |

[a] a-Si: amorphous Si, i: intrinsic; [b] KHP: potassium hydrogen phthalate; [c] KBi: potassium borate.

tee simultaneous antireflection and enhanced hydrophilicity.[12] Additionally, the larger surface area of nanostructured surface may result in a high density of defect states. Care must be taken to avoid extra bubble adhesion and surface recombination when designing the surface nanostructures for antireflection.

## 6. Summary and Outlook

Single-crystal semiconductors with narrow band gaps have shown great potentials for efficient solar water splitting (Table 1). Particularly, the thermodynamic instability of narrow-band-gap semiconductor could be overcome by depositing anti-corrosion layers with tunneling, conduction band transport, or defect-state transport mechanisms that ensured efficient conduction of photogenerated minority carriers. The sluggish $H_2$ and $O_2$ evolution kinetics on semiconductor surfaces can be largely accelerated by loading earth-abundant cocatalysts, such as $MoS_x$ and Ni-Mo alloy for the HER, as well as Co-$P_i$ and 3d transition-metal (Ni, Co, Fe, Mn) oxides for the OER. Forming buried p-n junctions, surface Schottky junctions, and backside Ohmic contacts are important approaches to enlarge the photovoltage generation, and ensure that photovoltage is essentially used to split water. Lastly, antireflection and improved wettability can be obtained by surface texturization of polished single-crystal substrates.

In spite of the above progresses, there are still many challenges and opportunities in designing narrow-band-gap semiconductors for solar water splitting. As shown in Table 1, although relatively high energy conversion efficiencies have been achieved for the HER half reaction, the OER part of water splitting is still low in efficiency. Thus, high performance OER cocatalysts and advanced electrode structures for photovoltage generation will continuously require extensive future investigations. In the fabrication of surface nanostructures or heavily doped shallow p-n junctions, it is desirable to explore more effective methods to avoid the use costly capital equipment such as photolithography tools, ion-implanters, or reactive ion etchers, to enable practical solar water splitting on a large scale. Additionally, it is desirable to develop cost-efficient methods to prepare multifunctional surface protective layers with catalytic activity, controlled energetics to form p-n junction or Schottky junction with the underlying semiconductor, and with an intermediate refractive index between the substrate and electrolyte for antireflection. In order to thoroughly understand the water splitting kinetics at atomic or molecular scales, in situ electrochemical measurement techniques with nanoscale spatial resolutions need to be applied to monitor the localized interfacial transfer processes of electrons and intermediates, such as scanning electrochemical microscopy (SECM) and electrochemical scanning tunneling microscopy (EC-STM).

*We acknowledge the National Natural Science Foundation of China (grant numbers 51302185, 21222604, and U1463205), the Specialized Research Fund for the Doctoral Program of Higher Education (grant numbers 20120032110024 and 20130032120018), the Scientific Research Foundation for the Returned Overseas Chinese Scholars (MoE), the Program of Introducing Talents of Discipline to Universities (B06006), and the Natural Science Foundation of Tianjin City (grant number 13JCYBJC37000) for financial support.*

**How to cite:** *Angew. Chem. Int. Ed.* **2015**, *54*, 10718–10732
*Angew. Chem.* **2015**, *127*, 10866–10881

[1] A. Fujishima, K. Honda, *Nature* **1972**, *238*, 37.
[2] M. G. Walter, E. L. Warren, J. R. McKone, S. W. Boettcher, Q. Mi, E. A. Santori, N. S. Lewis, *Chem. Rev.* **2010**, *110*, 6446.
[3] a) N. S. Lewis, D. G. Nocera, *Proc. Natl. Acad. Sci. USA* **2006**, *103*, 15729; b) A. Kudo, *MRS Bull.* **2011**, *36*, 32; c) T. Hisatomi, J. Kubota, K. Domen, *Chem. Soc. Rev.* **2014**, *43*, 7520.
[4] K. Sun, S. Shen, Y. Liang, P. E. Burrows, S. S. Mao, D. Wang, *Chem. Rev.* **2014**, *114*, 8662.
[5] L. Gao, Y. Cui, J. Wang, A. Cavalli, A. Standing, T. T. T. Vu, M. A. Verheijen, J. E. M. Haverkort, E. P. A. M. Bakkers, P. H. L. Notten, *Nano Lett.* **2014**, *14*, 3715.

  

[6] A. Heller, R. Vadimsky, *Phys. Rev. Lett.* **1981**, *46*, 1153.
[7] O. Khaselev, J. A. Turner, *Science* **1998**, *280*, 425.
[8] S. Licht, B. Wang, S. Mukerji, T. Soga, M. Umeno, H. Tributsch, *Int. J. Hydrogen Energy* **2001**, *26*, 653.
[9] D. M. Powell, M. T. Winkler, H. J. Choi, C. B. Simmons, D. B. Needleman, T. Buonassisi, *Energy Environ. Sci.* **2012**, *5*, 5874.
[10] M. A. Green, K. Emery, Y. Hishikawa, W. Warta, E. D. Dunlop, *Prog. Photovoltaics* **2015**, *23*, 1.
[11] a) S. W. Boettcher, E. L. Warren, M. C. Putnam, E. A. Santori, D. Turner-Evans, M. D. Kelzenberg, M. G. Walter, J. R. McKone, B. S. Brunschwig, H. A. Atwater, N. S. Lewis, *J. Am. Chem. Soc.* **2011**, *133*, 1216; b) B. Seger, A. B. Laursen, P. C. K. Vesborg, T. Pedersen, O. Hansen, S. Dahl, I. Chorkendorff, *Angew. Chem. Int. Ed.* **2012**, *51*, 9128; *Angew. Chem.* **2012**, *124*, 9262.
[12] Y. Hou, B. L. Abrams, P. C. K. Vesborg, M. E. Björketun, K. Herbst, L. Bech, A. M. Setti, C. D. Damsgaard, T. Pedersen, O. Hansen, J. Rossmeisl, S. Dahl, J. K. Nørskov, I. Chorkendorff, *Nat. Mater.* **2011**, *10*, 434.
[13] D. V. Esposito, I. Levin, T. P. Moffat, A. A. Talin, *Nat. Mater.* **2013**, *12*, 562.
[14] L. Ji, M. D. McDaniel, S. Wang, A. B. Posadas, X. Li, H. Huang, J. C. Lee, A. A. Demkov, A. J. Bard, J. G. Ekerdt, E. T. Yu, *Nat. Nanotechnol.* **2014**, *10*, 84.
[15] B. Seger, T. Pedersen, A. B. Laursen, P. C. K. Vesborg, O. Hansen, I. Chorkendorff, *J. Am. Chem. Soc.* **2013**, *135*, 1057.
[16] B. Seger, D. S. Tilley, T. Pedersen, P. C. K. Vesborg, O. Hansen, M. Grätzel, I. Chorkendorff, *RSC Adv.* **2013**, *3*, 25902.
[17] T. Wang, Z. Luo, C. Li, J. Gong, *Chem. Soc. Rev.* **2014**, *43*, 7469.
[18] M. G. Kast, L. J. Enman, N. J. Gurnon, A. Nadarajah, S. W. Boettcher, *ACS Appl. Mater. Interfaces* **2014**, *6*, 22830.
[19] Y. Lin, C. Battaglia, M. Boccard, M. Hettick, Z. Yu, C. Ballif, J. W. Ager, A. Javey, *Nano Lett.* **2013**, *13*, 5615.
[20] M. H. Lee, K. Takei, J. Zhang, R. Kapadia, M. Zheng, Y.-Z. Chen, J. Nah, T. S. Matthews, Y.-L. Chueh, J. W. Ager, A. Javey, *Angew. Chem. Int. Ed.* **2012**, *51*, 10760; *Angew. Chem.* **2012**, *124*, 10918.
[21] Y. Lin, R. Kapadia, J. Yang, M. Zheng, K. Chen, M. Hettick, X. Yin, C. Battaglia, I. D. Sharp, J. W. Ager, A. Javey, *J. Phys. Chem. C* **2015**, *119*, 2308.
[22] N. C. Strandwitz, D. J. Comstock, R. L. Grimm, A. C. Nichols-Nielander, J. Elam, N. S. Lewis, *J. Phys. Chem. C* **2013**, *117*, 4931.
[23] K. Sun, X. Pang, S. Shen, X. Qian, J. S. Cheung, D. Wang, *Nano Lett.* **2013**, *13*, 2064.
[24] a) J. J. H. Pijpers, M. T. Winkler, Y. Surendranath, T. Buonassisi, D. G. Nocera, *Proc. Natl. Acad. Sci. USA* **2011**, *108*, 10056; b) S. Y. Reece, J. A. Hamel, K. Sung, T. D. Jarvi, A. J. Esswein, J. J. H. Pijpers, D. G. Nocera, *Science* **2011**, *334*, 645; c) C. R. Cox, M. T. Winkler, J. J. H. Pijpers, T. Buonassisi, D. G. Nocera, *Energy Environ. Sci.* **2013**, *6*, 532.
[25] K. Sun, S. Shen, J. S. Cheung, X. Pang, N. Park, J. Zhou, Y. Hu, Z. Sun, S. Y. Noh, C. T. Riley, P. K. L. Yu, S. Jin, D. Wang, *Phys. Chem. Chem. Phys.* **2014**, *16*, 4612.
[26] Y. W. Chen, J. D. Prange, S. Dühnen, Y. Park, M. Gunji, C. E. D. Chidsey, P. C. McIntyre, *Nat. Mater.* **2011**, *10*, 539.
[27] M. J. Kenney, M. Gong, Y. Li, J. Z. Wu, J. Feng, M. Lanza, H. Dai, *Science* **2013**, *342*, 836.
[28] S. Hu, M. R. Shaner, J. a. Beardslee, M. Lichterman, B. S. Brunschwig, N. S. Lewis, *Science* **2014**, *344*, 1005.
[29] S. G. Kumar, K. S. R. K. Rao, *Energy Environ. Sci.* **2014**, *7*, 45.
[30] M. F. Lichterman, A. I. Carim, M. T. McDowell, S. Hu, H. B. Gray, B. S. Brunschwig, N. S. Lewis, *Energy Environ. Sci.* **2014**, *7*, 3334.
[31] A. B. Laursen, T. Pedersen, P. Malacrida, B. Seger, O. Hansen, P. C. K. Vesborg, I. Chorkendorff, *Phys. Chem. Chem. Phys.* **2013**, *15*, 20000.
[32] K. Sun, N. Park, Z. Sun, J. Zhou, J. Wang, X. Pang, S. Shen, S. Y. Noh, Y. Jing, S. Jin, P. K. L. Yu, D. Wang, *Energy Environ. Sci.* **2012**, *5*, 7872.
[33] J. Yang, K. Walczak, E. Anzenberg, F. M. Toma, G. Yuan, J. Beeman, A. Schwartzberg, Y. Lin, M. Hettick, A. Javey, J. W. Ager, J. Yano, H. Frei, I. D. Sharp, *J. Am. Chem. Soc.* **2014**, *136*, 6191.
[34] K. Sun, Y. Kuang, E. Verlage, B. S. Brunschwig, C. W. Tu, N. S. Lewis, *Adv. Energy Mater.* **2015**, *5*, 1402276.
[35] Y. Jiao, Y. Zheng, M. Jaroniec, S. Z. Qiao, *Chem. Soc. Rev.* **2015**, *44*, 2060.
[36] J. Ran, J. Zhang, J. Yu, M. Jaroniec, S. Z. Qiao, *Chem. Soc. Rev.* **2014**, *43*, 7787.
[37] J. Ran, J. Zhang, J. Yu, S. Z. Qiao, *ChemSusChem* **2014**, *7*, 3426.
[38] R. N. Dominey, N. S. Lewis, J. A. Bruce, D. C. Bookbinder, M. S. Wrighton, *J. Am. Chem. Soc.* **1982**, *104*, 467.
[39] B. Hinnemann, P. G. Moses, J. Bonde, K. P. Jorgensen, J. H. Nielsen, S. Horch, I. Chorkendorff, J. K. Nørskov, *J. Am. Chem. Soc.* **2005**, *127*, 5308.
[40] T. F. Jaramillo, K. P. Jørgensen, J. Bonde, J. H. Nielsen, S. Horch, I. Chorkendorff, *Science* **2007**, *317*, 100.
[41] J. R. McKone, E. L. Warren, M. J. Bierman, S. W. Boettcher, B. S. Brunschwig, N. S. Lewis, H. B. Gray, *Energy Environ. Sci.* **2011**, *4*, 3573.
[42] E. L. Warren, J. R. McKone, H. a. Atwater, H. B. Gray, N. S. Lewis, *Energy Environ. Sci.* **2012**, *5*, 9653.
[43] T. R. Cook, D. K. Dogutan, S. Y. Reece, Y. Surendranath, T. S. Teets, D. G. Nocera, *Chem. Rev.* **2010**, *110*, 6474.
[44] J. Yang, D. Wang, H. Han, C. Li, *Acc. Chem. Res.* **2013**, *46*, 1900.
[45] B. Mei, B. Seger, T. Pedersen, M. Malizia, O. Hansen, I. Chorkendorff, P. C. K. Vesborg, *J. Phys. Chem. Lett.* **2014**, *5*, 1948.
[46] M. W. Kanan, D. G. Nocera, *Science* **2008**, *321*, 1072.
[47] a) E. R. Young, D. G. Nocera, V. Bulović, *Energy Environ. Sci.* **2010**, *3*, 1726; b) E. R. Young, R. Costi, S. Paydavosi, D. G. Nocera, V. Bulović, *Energy Environ. Sci.* **2011**, *4*, 2058.
[48] R. D. Smith, M. S. Prevot, R. D. Fagan, Z. Zhang, P. A. Sedach, M. K. Siu, S. Trudel, C. P. Berlinguette, *Science* **2013**, *340*, 60.
[49] K. Jun, Y. S. Lee, T. Buonassisi, J. M. Jacobson, *Angew. Chem. Int. Ed.* **2012**, *51*, 423; *Angew. Chem.* **2012**, *124*, 438.
[50] H.-P. Wang, K. Sun, S. Y. Noh, A. Kargar, M.-L. Tsai, M.-Y. Huang, D. Wang, J.-H. He, *Nano Lett.* **2015**, *15*, 2817.
[51] Z. Zhang, J. T. Yates, *Chem. Rev.* **2012**, *112*, 5520.
[52] A. I. Hochbaum, P. Yang, *Chem. Rev.* **2010**, *110*, 527.
[53] S. Chattopadhyay, Y. F. Huang, Y. J. Jen, A. Ganguly, K. H. Chen, L. C. Chen, *Mater. Sci. Eng. R* **2010**, *69*, 1.

Received: April 13, 2015
Published online: July 23, 2015

  